



Classical vs. quantum plasmon-induced molecular transformations at metallic nanojunctions

Alexander B. C. Mantilla^a 📵, Chih-Feng Wang^b 📵, Andrey Krayev^c, Yi Gu^a, Zachary D. Schultz^d 📵, and Patrick Z. El-Khoury^{b.1} 📵

Edited by Catherine Murphy, University of Illinois at Urbana-Champaign, Urbana, IL; received November 2, 2023; accepted February 12, 2024

Chemical transformations near plasmonic metals have attracted increasing attention in the past few years. Specifically, reactions occurring within plasmonic nanojunctions that can be detected via surface and tip-enhanced Raman (SER and TER) scattering were the focus of numerous reports. In this context, even though the transition between localized and nonlocal (quantum) plasmons at nanojunctions is documented, its implications on plasmonic chemistry remain poorly understood. We explore the latter through AFM-TER-current measurements. We use two molecules: i) 4-mercaptobenzonitrile (MBN) that reports on the (non)local fields and ii) 4-nitrothiophenol (NTP) that features defined signatures of its neutral/anionic forms and dimer product, 4,4'-dimercaptoazobenzene (DMAB). The transition from classical to quantum plasmons is established through our optical measurements: It is marked by molecular charging and optical rectification. Simultaneously recorded force and current measurements support our assignments. In the case of NTP, we observe the parent and DMAB product beneath the probe in the classical regime. Further reducing the gap leads to the collapse of DMAB to form NTP anions. The process is reversible: Anions subsequently recombine into DMAB. Our results have significant implications for AFM-based TER measurements and their analysis, beyond the scope of this work. In effect, when precise control over the junction is not possible (e.g., in SER and ambient TER), both classical and quantum plasmons need to be considered in the analysis of plasmonic reactions

localized plasmons | quantum plasmons | plasmonic chemistry | tip-enhanced Raman

The resonant interaction between optical fields and metals can generate surface plasmons. When the metals of choice are nano-sized, i.e., much smaller than the wavelength of light used to excite them, the incident optical fields can be localized to their surfaces in the form of localized plasmons. These localized and enhanced optical fields are routinely used in measurement aimed at detecting and identifying (bio)molecules, with down to single-molecule detection sensitivity (1, 2). They have also been exploited to probe excitons and phonons in low-dimensional and quantum materials with nanometer spatial resolution (3). Localized surface plasmons have also been used to drive chemical transformations that are difficult to achieve using classical thermal/photochemical approaches (4, 5). The latter comprises the topic of this work.

From methyl migration (6) and CO₂ reduction (7) to redox reactions (8) through ethylene epoxidation and hydrogenation (9), plasmonic reactions performed under ambient conditions have the potential to decrease the energy demand and environmental bills that are associated with key industrial reactions. However, as well recognized in a recent account (5), the mechanisms that are associated with such reactions remain poorly understood. This limits our ability to rationally design plasmonic reactors and to scale up these reactions. Some of these challenges have to do with the very nature of the problem that lies at the interface of classical and quantum theories. Indeed, the dynamic interplay between a heterogeneous plasmonic metal and molecules under irradiation is not trivial to dissect in theory and in practice (10).

Surface-enhanced Raman [SER (11)] spectroscopy is a convenient approach that can be used to track chemical transformations at the surface of a plasmonic metal (5). Indeed, the same local fields that drive plasmonic chemistry boost the detection sensitivity of Raman scattering. The effect is most evident when molecules reside in nanosized (or smaller) cavities between two or more plasmonic nanostructures (4). When one of these nanostructures is a metallic probe of a scanning probe microscope, ultrasensitive nanoscale chemical (and chemical reaction) imaging becomes possible using the so-called tip-enhanced Raman [TER (12)] approach (4). Indeed, several reports from our group (13, 14) and others (4, 15, 16) showed that plasmonic reactions at metallic nanojunctions can be tracked via TER spectroscopy and imaging, with a spatial resolution down to a few nanometers under ambient laboratory conditions (10, 14).

Significance

We show that the transition from localized to quantum plasmons at metallic nanojunctions significantly affects local chemistry. Specifically, optical rectification and molecular charging in the tunneling regime lead to distinct reaction pathways and (redox) products. Our observations have more general implications for plasmonic (nano) reactor engineering and the analysis of ambient surface and tip-enhanced Raman spectra and images of molecules interacting with metals.

Author affiliations: aDepartment of Physics and Astronomy, Washington State University, Pullman, WA 99164; bPhysical Sciences Division, Pacific Northwest National Laboratory, Richland, WA 99352; ^cHoriba Instruments, Inc., Novato, CA 94949; and ^dDepartment of Chemistry and Biochemistry, The Ohio State University, Columbus, OH 43210

Author contributions: P.Z.E.-K. designed research; A.B.C.M. and A.K. performed research; C.-F.W., A.K., Y.G., Z.D.S., and P.Z.E.-K. contributed new reagents/analytic tools; A.B.C.M. and P.Z.E.-K. analyzed data; and A.B.C.M., C.-F.W., A.K., Y.G., Z.D.S., and P.Z.E.-K. wrote the paper.

Competing interest statement; Y.G. has has equity interest in Klar Scientific. Nothing else to report.

This article is a PNAS Direct Submission.

Copyright © 2024 the Author(s). Published by PNAS. This article is distributed under Creative Commons Attribution-NonCommercial-NoDerivatives License 4.0 (CC BY-NC-ND).

¹To whom correspondence may be addressed. Email: patrick.elkhoury@pnnl.gov.

This article contains supporting information online at https://www.pnas.org/lookup/suppl/doi:10.1073/pnas. 2319233121/-/DCSupplemental.

Published March 28, 2024.

The transition between classical and quantum plasmons as the distance between two plasmonic metals is decreased is somewhat well understood for idealized nanostructures (e.g., metallic spheres), as documented in pioneering theoretical and experimental work (17). Namely, classical plasmons that are localized to the nanojunction at separation distances >1 nm are replaced by nonlocal/charge shuttling quantum plasmons when conductive overlap is established at smaller sub-nm separation distances. How the nonlocal character of quantum plasmons affects the properties of molecular and material systems at plasmonic junctions remains poorly understood, besides a handful of analyses (18-22). In the realm of plasmonic chemistry, the topic of this work, none of the existing analyses take the transition from classical to quantum plasmons into account. This is surprising, especially since assemblies of interacting plasmonic nanoparticles would be needed to scale up plasmonic catalysis (23). This work sheds light on important aspects of this problem through simultaneously recorded AFM-TER-current measurements that track chemistry driven by both local and nonlocal plasmons in the tip-enhanced optical spectroscopy geometry. Even though the optical data can be understood in the framework of prior experimental SER and TER studies (discussed below), simultaneously recorded force and current signals are useful to gauge the tip-sample distance and to establish the tunneling regime. We begin with a brief description of our experimental construct.

Results

Simultaneously recorded AFM (A), TER (B), and current (C) images of a 4-mercaptobenzonitrile (MBN)-coated gold nanohole are shown in Fig. 1. We thoroughly characterized similar hybrid molecular-metallic constructs in recent publications from our group (24, 25). The reader is referred to the prior analyses for a more detailed description of the substrate and laterally resolved mapping measurements. For this study, the topography of the ~19 nm deep oval nanostructure is well-resolved in the AFM image (Fig. 1A) and the overlaid cross-sectional cut. The TER (Fig. 1B) and current (Fig. 1C) maps both reveal regions of high optical field enhancement under our experimental conditions. Spatial averaging over the highlighted rectangular area in Fig. 1B yields the optical response plotted in Fig. 1D. The spectrum exhibits several sharp molecular lines that can be assigned to MBN, including the 1,580/2,225 cm⁻¹ resonances that arise from the aromatic C=C/nitrile stretching vibrations. Averaging the TER signal along the horizontal lines near the upper right corner of the rectangle in Fig. 1B yields the cross-sectional line profile plotted in Fig. 1E. As expected, this trace reveals that the spatial resolution is finer than the lateral step size used in this map. Indeed, similar measurements performed using smaller lateral steps (SI Appendix, Fig. S1) show that our spatial resolution is closer to 2 nm, which is consistent with prior estimates from measurements that targeted similar plasmonic constructs (25).

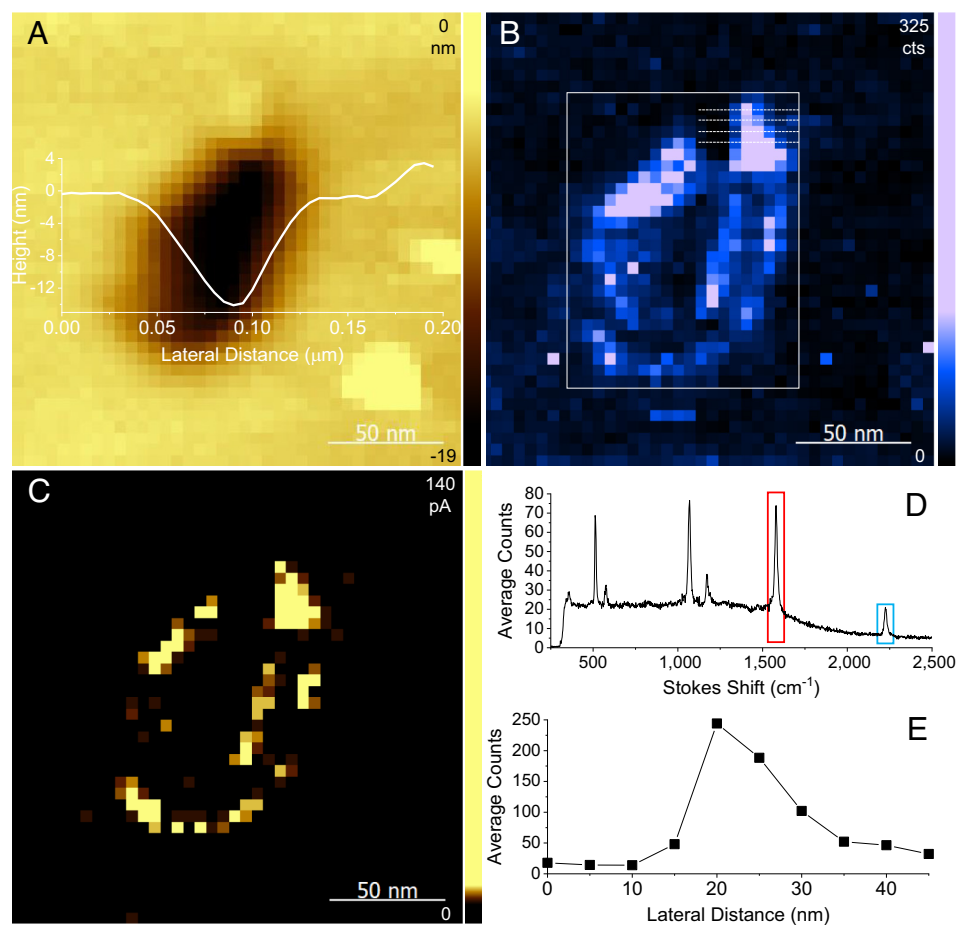


Fig. 1. Correlated AFM (*A*), TER (*B*), and current (*C*) images of an Au nanohole (see ref. 24 for a description and ref. 25 for high spatial resolution imaging of similar structures), herein coated with 4-mercaptobenzonitrile molecules. Spatial averaging of the TER response in the rectangular area in (*B*) results in the spectrum plotted in (*D*). Spatially averaged TER cross-sectional line cuts (1,580 cm⁻¹) along the dashed horizontal lines in (*B*) results in the line cross-sectional profile shown in (*E*). Finer spatial resolution (~2 nm) is demonstrated in *SI Appendix*, Fig. S1 of the *SI Appendix* section through TER maps recorded with fine lateral step sizes (1 nm). Conditions: 0.5 s integration time/pixel, 5 nm steps in both lateral directions, and 100 μW/μm² delivered to the tip-sample nanojunction.

We next recorded TER, AFM force, and current signals while continuously decreasing the distance between the AFM probe and sample, as schematically illustrated in Fig. 2A. The tip is landed toward the edge of the nanohole structure, where the optical signals are optimally enhanced (Fig. 1B). The rapid onset of TER signal enhancement (~2 nm rise) is noticeable in the spectrally resolved map (Fig. 2B) and more so in the two TER cuts in Fig. 2D. The tip-sample separation distance is however difficult to establish based on these optical signals alone. The AFM force distance curve in Fig. 2C and simultaneously recorded current trace in Fig. 2E are informative in this regard. The force–distance curve clearly shows the snap-to-contact point, where the gradient of the tip-sample force exceeds the elastic constant of the cantilever and the tip snaps into contact with the surface. After contact, the tip and the sample motion are linearly coupled, and the onset of the local repulsive force is accompanied by a rise in both optical and current signals. The offset between the vdW contact point (0 nm in C) and the rise in Raman scattering and current suggests that the tip and sample are still separated (vide infra) by molecules in the junction—both MBN as well as other molecules present under ambient conditions, such as water molecules (21). The decrease in current after it reaches a maximum value at -5 nm (conductive contact) can be simply associated with changes in the tip/sample morphology and variations in the number of molecules at the junction. That said, and as shown below, it is not the case. Namely, we can associate this reproducible (SI Appendix, Fig. S2) observation with half-wave optical rectification at plasmonic junctions, which has been previously observed in the TER geometry (20, 26, 27). More in support of this assignment follows.

The reproducibility of the measurements discussed above was ensured by recording AFM–TER–current traces as a function of gap size at several points along the periphery of the nanohole using different TER probes (*SI Appendix*, Fig. S2). In Fig. 3, we show one of these measurements and focus our analysis of the optical signal to a narrow spectral region centered around the nitrile stretching resonance of MBN. Offset AFM force–distance (Fig. 3A) and current (Fig. 3B) signals that track vdW (0 nm in A and B) and conductive contact (around –4.5 nm in A and B), respectively, are once again observed. The spectrally resolved optical signal in the 2,150 to 2,300 cm⁻¹ spectral region is consistent

with the picture painted by the results in Fig. $3\,A$ and B. Namely, we observe two maxima in the TER signature of the nitrile—the first at -2 nm and a second at -7 nm. We also clearly observe the transition from a sharp molecular line that peaks at the first maximum to a Stark-broadened nitrile signature that peaks at the second. The transition in the nature of the optical signal happens at around -5 nm, wherein conductive contact is established (Fig. 3B) and where the actual tip—sample separation distance is known to be less than 1 nm (21). Again, the optical data that can be rationalized in the framework of prior work (18, 28) is supported by the simultaneously recorded force and current measurements.

The observation of two signal maxima in the TER data (see, e.g., Fig. 3) can be associated with classical vs. quantum plasmon-enhanced Raman scattering. In effect, the transition from sharp molecular lines to Stark-tuned broadened Raman signatures has been previously observed in the SER spectra of a melting plasmonic metal dimer and rationalized on this basis (18). In the current geometry, we can controllably access the two regimes and explore them using different molecular reporters that inform on the operative fields (Fig. 3) and on plasmonic chemistry (Fig. 4). Before discussing an example of plasmonic chemistry, it is important to comment on the signal magnitudes that do not trace the expected field profile (28). Specifically, as the distance between two plasmonic nanostructures is decreased, the field should increase until it reaches a critical separation distance (sub-nm) after which enhancement decreases as a result of quantum effects such as tunneling (17). What we observe is a brighter quantum-plasmon-enhanced TER signal and a dimmer localized junction plasmon-driven TER signal at a larger tip-sample separation distance. A closer inspection of the Raman lines of MBN (SI Appendix, Fig. S3) reveals that the molecule is charged. Although the latter is masked in the nitrile window, where optical rectification and (partial) molecular charging both affect the observables (29), charging is clearly marked by an 8 cm⁻¹ blue shift in the resonance of the aromatic C=C vibrational signature of MBN, see SI Appendix, Fig. S3. It appears that an increase in the Raman scattering cross-section of the anion competes with the expected dimming of the field magnitude in the tunneling regime.

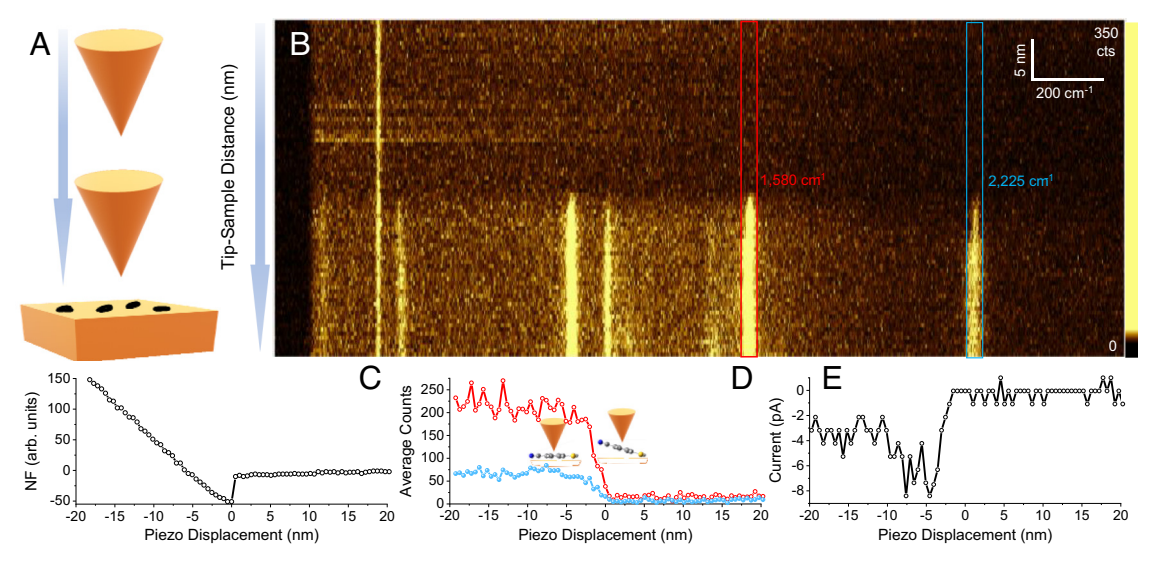


Fig. 2. Schematic representation of the measurement (*A*) is shown alongside the tip–sample distance-dependent spectrally resolved TER response (*B*). AFM force (*C*), selected frequency TER cuts (*D*, color coded in *B*), and current signals (*E*) are all simultaneously tracked. Note that the spectral response in (*C*) is integrated over the bands, as schematically illustrated by the color-coded thin rectangular sections in (*B*). Conditions: 0.5 s integration time/step, 0.5 nm steps, and 100 μ W/ μ m² delivered to the tip–sample nanojunction. Note that a small bias voltage of 0.018 V was used in this measurement.

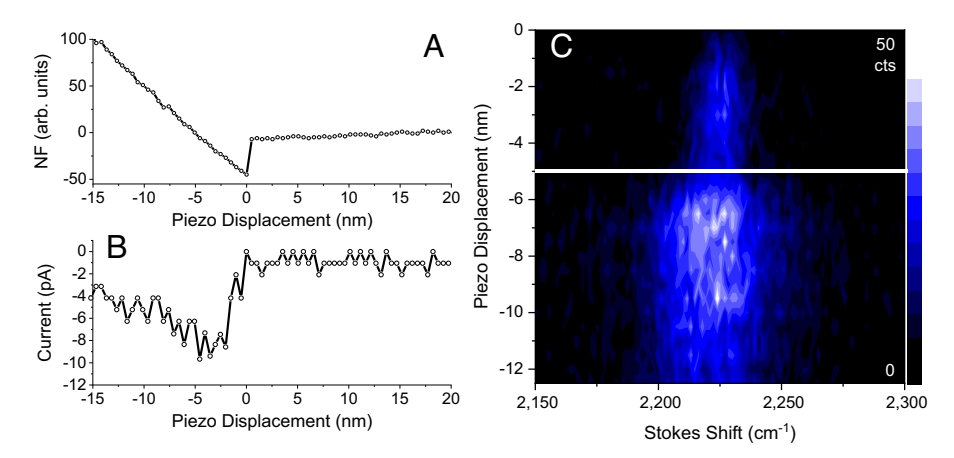


Fig. 3. Force (A), current (B), and TER (C) in the 2,150 to 2,300 cm⁻¹ spectral range are shown. The same behavior described in Fig. 2 is once again observed in (A) and (B), recorded at a different point along the edge of the nanohole visualized in Fig. 1. Except for the probe, the measurement conditions used here are identical to those in Fig. 2. See text for more details.

Based on the results shown in Fig. 3C, we can place an upper limit of ~42 MVcm⁻¹ for the magnitude of the rectified local optical field. This is based on a stark tuning rate of 0.6 cm⁻¹/ MVcm⁻¹ for the neutral molecule and the lowest observed nitrile frequency shift of 2,200 cm⁻¹ (22). The derived magnitude does not account for molecular charging, which is clearly taking place under our experimental conditions, see SI Appendix, Fig. S3. The Stark tuning rate for the anion was recently computed to be 0.54 cm⁻¹/MVcm⁻¹ (30). This translates into a local field magnitude

of ~46 MVcm⁻¹, if we assume that the charged molecules account for the lowest observed frequency shifts. Overall, the absolute field magnitudes derived here are generally consistent with rectified local field magnitudes in the TER geometry (30, 31). Note that these values do not account for static charge transfer and/or conformational fluxionality/conformations of molecules on metals, both which are not expected to significantly affect the nominal nitrile resonance (32). That large rectified optical fields are operative is an important observation to keep in mind, since rectified

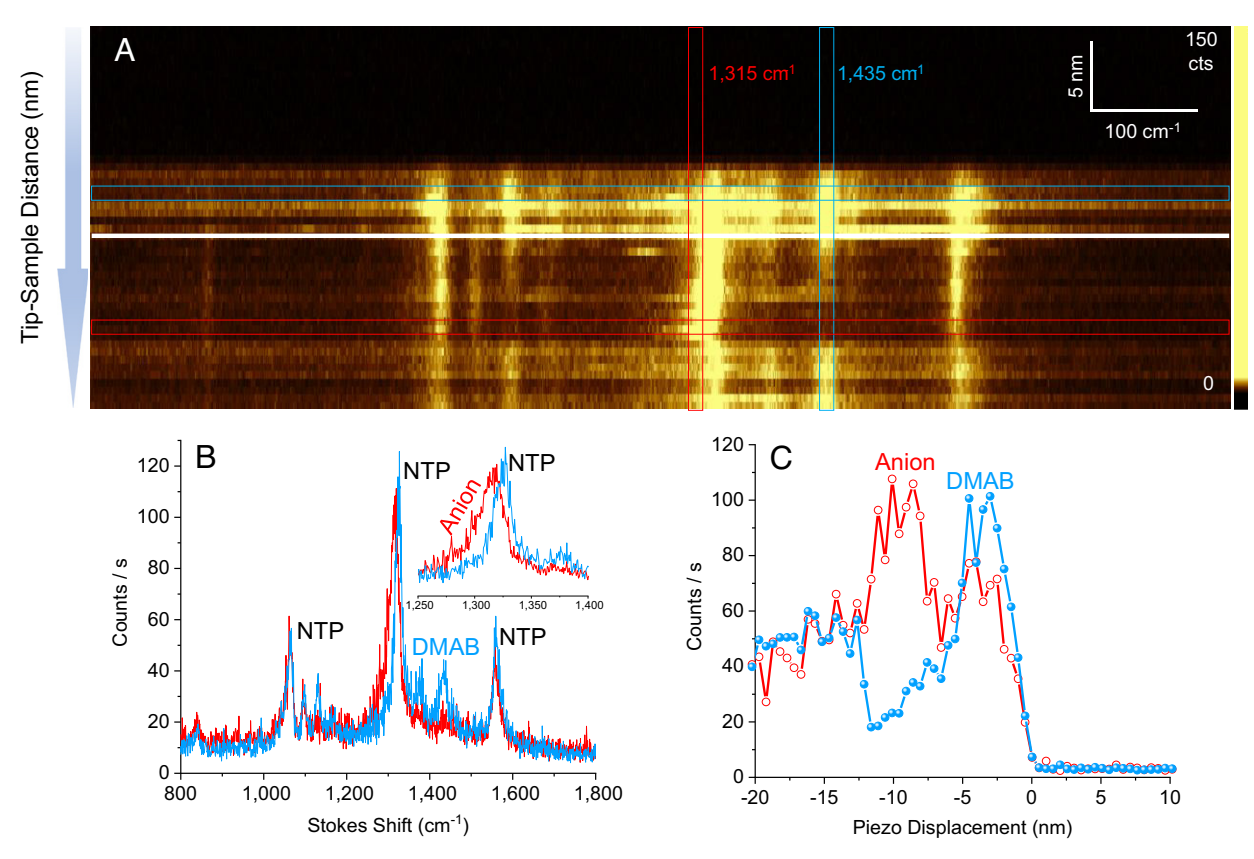


Fig. 4. The measurements that were performed for MBN above were repeated, but now using 4-nitrothiophenol as a reporter. The tip-sample distance-dependent spectrally resolved TER response is shown in (A), and cuts along the horizontal (B) and vertical (C) directions are shown. Note that cuts in both directions are averaged over the highlighted widths of the vertical/horizontal triangular areas in (A). Conditions: 0.5 s integration time/step, 0.5 nm steps, and 100 µW/µm² delivered to the tip-sample nanojunction. Note that a small bias voltage of 0.018 V was used in this measurement for overall consistency.

fields have been shown to affect plasmonic reactivity (27, 33), which we take a closer look at next.

The measurements highlighted above were repeated in Fig. 4, but now using 4-nitrothiophenol (NTP) molecules that are well-known reporters of local redox and bimolecular chemistry in SER and TER measurements. Spectral variations throughout the transition from classical to quantum plasmon-enhanced TER scattering are evident in Fig. 4A. The spectra we observe in the two limits are overlaid in Fig. 4B. In the classical regime, both parent NTP molecules as well as 4,4'-dimercaptoazobenzene contribute to the spectrum. The latter is marked by several peaks among which the 1,435 and 1,390 cm⁻¹ modes that involve the azo moiety are most prominent (13). After the onset of tunneling, a clear signature of anionic NTP species is observed at 1,315 cm (20, 34, 35). The signature of the anion is highlighted in the *Inset* of Fig. 4B, and it is consistent with prior assignments of anionic NTP species in conventional and electrochemical TER measurements (20, 34, 35). An interesting aspect of the local chemistry is highlighted in Fig. 4C, wherein we track the evolution of the DMAB and anionic NTP species through their prominent TER signatures. Much like the case of MBN, the rise in the TER signals of the parent NTP species (and the DMAB product, see Fig. 4C) starts after vdW contact, reaches a maximum value at around -3 nm, and then decays and to reach a local minimum below -5 nm. The decay of the DMAB product leads to an increase in anionic NTP species (Fig. 4C). Interestingly, the process is reversible. Namely, the anions eventually recombine to once again form DMAB. The reproducibility of these observations is again ensured using measurements conducted with different tips that target different areas on the substrate, as exemplified by the results shown in SI Appendix, Fig. S4.

Discussion

Several conclusions seem inescapable based on our observations. First, both classical and quantum plasmons contribute to tipenhanced optical nanoimaging and nanospectroscopy measurements that take advantage of plasmonic junctions to optimally enhance the incident and scattered fields. Beyond the well-known fact that quantum plasmons are operative in smaller gaps (17, 21), this work establishes that quantum plasmons are operative whenever the force is positive or exceeds the contact line (Figs. 2–4) in AFM-TER measurements. It is likely for the picture to also depend on the molecular/material load as well as the power of the incident field. In this regard, dozens of recent TER and tipenhanced photoluminescence studies that utilize plasmonic junctions to inspect low dimensional and quantum material need to be revisited and re-analyzed with quantum plasmons and the possibility of charging in mind. Second, it appears that only tunneling plasmons are rectified. This is an interesting observation to keep in mind, since correlated current-optical-force measurements that all support the mechanisms proposed herein may not be possible, e.g., in the SER scheme. In this regard, optical measurements performed with strategic molecular probes (e.g., MBN) may be used to infer the (non)local nature of the operative field. In this study, both the observation of Stark broadened nitrile resonances and the reduction in current that converges to half its value after conductive contact is established point toward optical rectification of quantum plasmons. Third, we demonstrate that molecular charging takes place in the TER geometry, and that it is most prominent in the tunneling regime. In the context of plasmonic chemistry, reaction pathways that involve both neutral and anionic species are therefore important to consider. Here, we show that the DMAB species that forms as a result of reductive

coupling between two NTP molecules can reversibly form anionic NTP species. The latter has not been considered in dozens of prior reports that take advantage of junction plasmons to track and better understand plasmonic chemistry, using NTP as a model system.

On a more technical note, this work suggests that further developments are warranted to render TER measurements more analytical and less invasive in nature. Performing mapping with negative force below the contact point should enhance the signatures of the molecule/material systems using classical/localized plasmons without perturbing the analytes, either mechanically or through redox chemistry. This work also motivates designing unique plasmonic reactors that take full advantage of the distinct properties of tunneling plasmons. It also beckons revisiting spectroscopic SER and TER measurements that are aimed at tracking chemical transformations, with attention to both anionic molecular species and quantum plasmons. The same goes for nanoimaging measurements that are aimed at characterizing emerging low-dimensional materials, where the same mechanisms must be operative and where, e.g., both excitons and trions can contribute to the recorded spectral images.

On a final note, it is important to concede that this work does not rigorously answer outstanding questions that have to do with the resonances of classical vs. quantum plasmons in the TER geometry and how that affects local chemistry. Addressing these questions requires nanoextinction measurements coupled with quantum or quantum-corrected numerical simulations of the local fields. Although this seems doable experimentally with some improvements in our current approach (36), going beyond separate treatments of the molecular and metallic constituents in silico requires more substantial work.

Materials and Methods

Our TER setup is described elsewhere in more detail (24, 25). For the purpose of this work, as-purchased silicon probes (Nanosensors, ATEC) were coated with 100 nm of Au and used for AFM and TER (SpecTop, Horiba Scientific) topographic/ chemical imaging as well as current mapping. TER and current signals are collected when the tip is in direct contact with the surface. A semicontact mode is otherwise used to move the sample relative to the tip (pixel to pixel). Throughout, a 633 nm diode laser is focused onto the tip apex at a ~65° angle with respect to the surface normal using a 100 × air objective (Mitutoyo, 0.7 NA). The polarization of the laser was set to coincide with the tip axis using a half-waveplate. The backscattered light was collected using the same objective, filtered through a series of long pass/dichroic filters, and recorded using a CCD camera (Andor, Newton EMCCD) coupled to a spectrometer (Andor, Shamrock 500) equipped with a 300 L/mm grating blazed at 550 nm. Note that the experimental details (irradiance, step sizes, integration time...) are given in figure captions in the main text.

TERS samples were prepared by immersing template stripped gold substrates in 1 mM ethanolic solutions of MBN and NTP for 24 h. Excess/unbound molecules on each of the two substrates were rinsed off using excess ethanol, and the final samples were dried using a stream of dry nitrogen.

Data, Materials, and Software Availability. The data needed to reproduce the figures are included with the SI Appendix section of this work. All other data are included in the manuscript and/or supporting information.

ACKNOWLEDGMENTS. A.B.C.M. and Y.G. acknowledge the support from the NSF (DMR-2004655). C.-F.W. was supported by the U.S. Department of Energy, Office of Science, Office of Biological and Environmental Research, through the bioimaging technology development program. Z.D.S. acknowledges the support from the NIH award R01 GM109988. P.Z.E.-K. acknowledges the support from the U.S. Department of Energy, Office of Science, Basic Energy Sciences, Chemical Sciences, Geosciences, and Biosciences Division, Condensed Phase, and Interfacial Molecular Science program, FWP 16248.

- E. C. Le Ru, P. G. Etchegoin, Single-molecule surface-enhanced Raman spectroscopy. Annu. Rev. Phys. Chem. 63, 65-87 (2012).
- A. B. Zrimsek et al., Single-molecule chemistry with surface- and tip-enhanced raman spectroscopy. Chem. Rev. 117, 7583-7613 (2017).
- J. Shao, W. Su, Tip-enhanced nanoscopy of two-dimensional transition metal dichalcogenides: Progress and perspectives. Nanoscale 14, 17119–17133 (2022).
- Z. Li, D. Kurouski, Plasmon-driven chemistry on mono- and bimetallic nanostructures. Acc Chem. Res. 54, 2477-2487 (2021).
- C. L. Warkentin, Z. Yu, A. Sarkar, R. R. Frontiera, Decoding chemical and physical processes driving plasmonic photocatalysis using surface-enhanced raman spectroscopies. Acc Chem. Res. 54, 2457–2466 (2021)
- J. L. Brooks, C. L. Warkentin, D. V. Chulhai, J. D. Goodpaster, R. R. Frontiera, Plasmon-mediated intramolecular methyl migration with nanoscale spatial control. ACS Nano 14, 17194–17202 (2020).
- E. Landaeta, N. I. Kadosh, Z. D. Schultz, Mechanistic study of plasmon-assisted photoelectrochemical CO₂ reduction to Acetate with a Ag/Cu₂O nanodendrite electrode. ACS Catal. 13, 1638–1648 (2023), 10.1021/acscatal.2c05082.
- A. Gelle et al., Applications of plasmon-enhanced nanocatalysis to organic transformations. Chem. Rev. 120, 986–1041 (2020).
- H. K. Choi et al., Metal-catalyzed chemical reaction of single molecules directly probed by vibrational spectroscopy. J. Am. Chem. Soc. 138, 4673-4684 (2016).
- P. Z. El-Khoury, Tip-enhanced Raman scattering on both sides of the Schro"dinger equation. Acc. Chem. Res. 54, 4576-4583 (2021).
- P. L. Stiles, J. A. Dieringer, N. C. Shah, R. R. Van Duyne, Surface-enhanced Raman spectroscopy. Annu. Rev. Anal. Chem. 1, 601-626 (2008).
- R. M. Stockle, Y. D. Suh, V. Deckert, R. Zenobi, Nanoscale chemical analysis by tip-enhanced Raman spectroscopy. Chem. Phys. Lett. 318, 131–136 (2000).
- A. Bhattarai, P.Z. El-Khoury, Nanoscale chemical reaction imaging at the solid-liquid interface via TERS. J. Phys. Chem. Lett. 10, 2817–2822 (2019).
- P. Z. El-Khoury, Tip-enhanced Raman chemical and chemical reaction imaging in H(2)O with sub-3nm spatial resolution. J. Am. Chem. Soc. 145, 6639-6642 (2023).
- P. Singh, T. Deckert-Gaudig, Z. Zhang, V. Deckert, Plasmon induced deprotonation of 2-mercaptopyridine. *Analyst* 145, 2106-2110 (2020).
- J. Szczerbinski, L. Gyr, J. Kaeslin, R. Zenobi, Plasmon-driven photocatalysis leads to products known from E-beam and X-ray-induced surface chemistry. Nano Lett. 18, 6740-6749 (2018).
- W. Zhu et al., Quantum mechanical effects in plasmonic structures with subnanometre gaps. Nat. Commun. 7, 11495 (2016).
- M. Banik et al., Surface-enhanced Raman trajectories on a nano-Dumbbell: Transition from field to charge transfer plasmons as the spheres fuse. Acs Nano 6, 10343–10354 (2012).
- P. Z. El-Khoury, D. H. Hu, V. A. Apkarian, W. P. Hess, Raman scattering at plasmonic junctions shorted by conductive molecular bridges. *Nano Lett.* 13, 1858–1861 (2013).

- C. F. Wang et al., Suppressing molecular charging, nanochemistry, and optical rectification in the tip-enhanced Raman geometry. J. Phys. Chem. Lett. 11, 5890–5895 (2020).
- Y. Zhang et al., Improving resolution in quantum subnanometre-gap tip-enhanced Raman nanoimaging. Sci. Rep. 6, 25788 (2016).
- H. Wang, K. Yao, J. A. Parkhill, Z. D. Schultz, Detection of electron tunneling across plasmonic nanoparticle-film junctions using nitrile vibrations. *Phys. Chem. Chem. Phys.* 19, 5786–5796 (2017).
- S. Lee et al., Controlled assembly of plasmonic nanoparticles: From static to dynamic nanostructures. Adv. Mater 33, e2007668 (2021).
- A. B. C. Mantilla, C. F. Wang, Y. Gu, Z. D. Schultz, P. Z. El-Khoury, Multipolar Raman scattering vs. interfacial nanochemistry: Case of 4-mercaptopyridine on gold. J. Am. Chem. Soc. 144, 20561–20565 (2022).
- C. F. Wang, B. T. O'Callahan, A. Krayev, P. Z. El-Khoury, Nanoindentation-enhanced tip-enhanced Raman spectroscopy. J. Chem. Phys. 154, 241101 (2021).
- K. T. Crampton, J. Lee, V. A. Apkarian, Ion-selective, atom-resolved imaging of a 2D Cu(2)N insulator: Field and current driven tip-enhanced Raman spectromicroscopy using a molecule-terminated tip. ACS Nano 13, 6363-6371 (2019).
- Z. D. Li, J. Rigor, N. Large, P. Z. El-Khoury, D. Kurouski, Underlying mechanisms of hot carrier-driven reactivity on bimetallic nanostructures. J. Phys. Chem. C. 125, 2492–2501 (2021).
- W. O. Zhu et al., Quantum mechanical effects in plasmonic structures with subnanometre gaps. Nat. Commun. 7, 11495 (2016).
- Y. Li et al., Interplay of bias-driven charging and the vibrational stark effect in molecular junctions. Nano Lett. 16, 1104-1109 (2016).
- A. Bhattarai et al., A closer look at corrugated Au tips. J. Phys. Chem. Lett. 11, 1915–1920 (2020).
- (2020).
 31. P. Z. El-Khoury, High spatial resolution ambient tip-enhanced (multipolar) Raman scattering. *Chem.*
- Commun. **59**, 3536–3541 (2023).
 32. A. Bhattarai *et al.*, Tip-enhanced Raman nanospectroscopy of smooth spherical gold nanoparticles. *J. Phys. Chem. Lett.* **11**, 1795–1801 (2020).
- D. A. Nelson, Z. D. Schultz, Influence of optically rectified electric fields on the plasmonic photocatalysis of 4-nitrothiophenol and 4-aminothiophenol to 4,4-dimercaptoazobenzene. J. Phys. Chem. C. 122, 8581-8588 (2018).
- C. F. Wang, B. T. O'Callahan, D. Kurouski, A. Krayev, P. Z. El-Khoury, The prevalence of anions at plasmonic nanojunctions: A closer look at p-nitrothiophenol. J. Phys. Chem. Lett. 11, 3809–3814 (2020)
- S. C. Huang et al., Probing the intermediate in the electrochemical reduction of nitrobenzene derivative by EC-TERS. J. Phys. Chem. C 127, 12568–12575 (2023).
- C. F. Wang, A. V. Krayev, P. Z. El-Khoury, Subnanometer visualization of spatially varying local field resonances that drive tip-enhanced optical spectroscopy. *Nano Lett.* 23, 9114–9118 (2023).